Ultrathin $Li_{1.3}Al_{0.3}Ti_{1.7}(PO_4)_3$-Based Flexible Solid Electrolyte for All-Solid-State Lithium Batteries

Jia Wang(王佳) [a], Hao He(何豪) [a]* and Zhendong Li(李振东) [b]*

[a] *School of Physics and Laboratory of Zhongyuan Light, Zhengzhou University, Zhengzhou 450001, China*

[b] *Key Laboratory of Flexible Optoelectronic Materials and Technology, Ministry of Education, School of Optoelectronic Materials & Technology, Jianghan University, Wuhan 430056, China*

Corresponding author: hehao@zzu.edu.cn and lizhendong@jhun.edu.cn

Abstract

NASICON-type solid electrolytes are highly attractive for solid-state lithium batteries due to their superior ionic conductivity and low cost. However, practical implementation remains severely limited by their inherent brittleness, poor solid-solid contact, and severe side reactions with lithium metal. Herein, we report a flexible $Li_{1.3}Al_{0.3}Ti_{1.7}(PO_4)_3$ (LATP)-based composite solid electrolyte film fabricated via an *in-situ* polymerization strategy. This film achieves an exceptionally high LATP loading of 90 wt% within a minimal thickness of 20 μm, ensuring outstanding thermal stability and safety. Crucially, the composite electrolyte delivers a competitive room-temperature ionic conductivity of 1.5×10^{-4} S cm^{-1} and an expansive electrochemical window exceeding 5.1 V. Consequently, symmetric Li||Li cells demonstrate excellent interfacial stability, sustaining over 600 hours of steady cycling at 60 °C and 0.1 mA cm^{-2}. Furthermore, full cells paired with LFP and NCM811 cathodes display superior long-term cyclability and rate performance.

Keywords: solvent-free, initiator-free, *in-situ* polymerization

PACS: 82.47.Aa (Lithium-ion batteries)
65.40.gk (Electrochemical properties)
82.45.Gj (Electrolytes)

1. Introduction

Lithium-ion batteries currently dominate the energy storage market owing to their high energy density, low self-discharge rate, and excellent environmental adaptability. However, the surging demand for higher energy densities in sectors like electric vehicles has gradually exposed the performance limits of traditional graphite anodes. In this context, lithium metal anodes are widely considered the most promising strategy to overcome this energy density bottleneck [1-5]. Nevertheless, the

use of conventional organic liquid electrolytes with lithium metal triggers critical issues. These include the uncontrolled proliferation of lithium dendrites, shortened cycle lifespans, and severe safety hazards. Consequently, these formidable challenges severely restrict the practical implementation and further development of lithium metal batteries [6-9].

To address these challenges, researchers have focused on developing solid-state lithium batteries utilizing solid-state electrolytes, such as polymers and inorganic ceramics. This strategy not only promises higher energy densities but also fundamentally ensures the safety of the batteries [10-12]. However, polymer electrolytes face distinct limitations. They are highly susceptible to decomposition at high voltages. This degradation is typically triggered by oxygen release from oxide cathodes, which ultimately degrades the interfacial performance [13]. On the other hand, inorganic solid electrolytes struggle with their own practical hurdles. Their extreme rigidity and excessive thickness make them difficult to process. Consequently, they suffer from inadequate solid-solid interfacial contact with the electrodes [14, 15].

Composite solid electrolytes, by integrating polymers with inorganic solid electrolytes, introduce flexible polymer components. This approach improves interfacial contact while preserving the excellent electrochemical stability, mechanical strength, and thermal stability of the inorganic electrolytes [16, 17]. Chen et al. [18] and Huo et al. [19] respectively reported a micrometer-scale polymer-ceramic composite electrolyte containing 80 wt% garnet ceramic, and a composite electrolyte with a thickness of approximately 60 μm containing 80 vol% $Li_{6.4}La_3Zr_{1.4}Ta_{0.6}O_{12}$ particles. Both employ poly (ethylene oxide) (PEO) as the polymer matrix. Owing to its favorable interfacial compatibility with lithium anodes, PEO has consistently been regarded as an ideal matrix material [20]. However, as the PEO content decreases, the flexibility of the composite electrolyte degrades significantly, even leading to brittle fracture.

On the other hand, due to the limited intrinsic ionic conductivity of the PEO matrix, the addition of plasticizers is generally required to reduce the crystallinity of PEO and thereby enhance conductivity. Among these, triethyl phosphate (TEP) is considered a highly desirable plasticizer because the high polarity of its –P=O group enables the dissolution of various lithium salts, endowing the electrolyte with high ionic conductivity and excellent flame retardancy [21]. Nevertheless, free TEP

molecules exhibit poor stability at both the cathode and anode interfaces, making them prone to triggering irreversible interfacial corrosion. This severely impairs the cycling performance of the battery and restricts further improvements in energy density [22]. Furthermore, such composite electrolytes are typically fabricated via the slurry casting method. This technique necessitates the use and evaporation of substantial amounts of organic solvents, which easily causes environmental pollution; concurrently, inorganic particles are prone to agglomeration during the preparation process, thereby compromising the structural uniformity of the electrolyte membrane.

In this study, a flexible and ultra-thin (20 μm) LATP-based film was successfully fabricated via an *in-situ* forming and subsequent curing approach. This membrane achieves a high ceramic content of 90% and delivers a room-temperature ionic conductivity of 1.5×10^{-4} S cm^{-1}. Furthermore, the *in-situ* curing process effectively locks the TEP within the electrolyte to restrict its mobility, thereby preventing continuous side reactions with the lithium metal. Concurrently, an integrated electrolyte/cathode interface was constructed. This overall design facilitates the uniform formation of the solid electrolyte interphase (SEI) and suppresses the uncontrolled growth of lithium dendrites. Benefiting from the aforementioned structural designs, the assembled Li||LFP and Li||NCM811 cells both exhibit outstanding cycling stability and rate performance at 60 °C.

2. Results and discussion

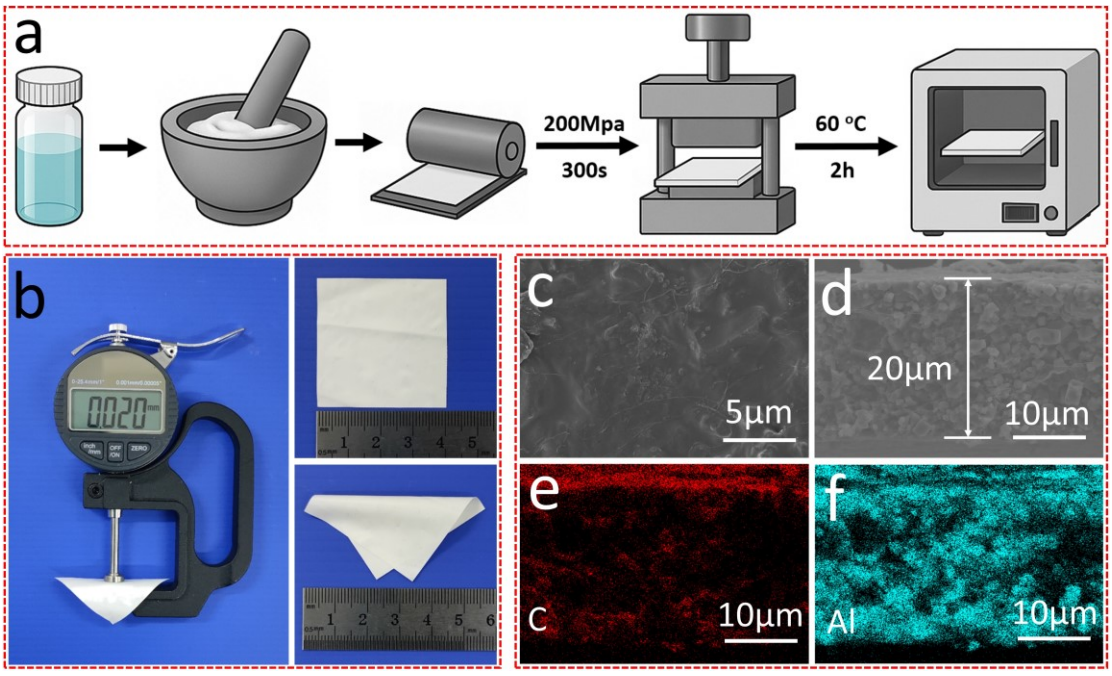


Fig. 1 (a) Schematic illustration of the synthesis route for the LATP-based film; (b) Thickness

measurement and digital photograph of the LATP-based film; (c) Surface and (d) cross-sectional scanning electron microscopy (SEM) images of the LATP-based film; and the corresponding energy-dispersive X-ray spectroscopy (EDS) elemental mapping of (e) Carbon and (f) Aluminum.

The synthesis procedure of the LATP-based film is illustrated in Fig. 1a. Initially, lithium bis(trifluoromethanesulfonyl)imide (LiTFSI) and lithium nitrate ($LiNO_3$) were thoroughly dissolved in poly(ethylene glycol) diglycidyl ether (PEGDE) and triethyl phosphate (TEP). Subsequently, LATP powder and diethylenetriamine (DETA) were further mixed with the aforementioned solution to yield a highly plastic elastomer mixture. The elastomer mixture was then processed through a roller press to achieve an appropriate thickness. Finally, following isostatic pressing and thermal curing treatments, an ultra-thin LATP-based film with a thickness of only 20 μm was obtained (Fig. 1b). Furthermore, owing to the presence of the polymer network, the LATP-based film also exhibits excellent flexibility and mechanical strength. As shown in Fig. S1a, the ultrathin membrane exhibits a tensile strength of ~0.22 MPa and an elongation at break of ~4.4%. Despite the extreme 90 wt% LATP loading, it maintains reliable mechanical robustness. The *in-situ* polymerized matrix successfully builds a flexible continuous network among the dense particles. This structure fundamentally overcomes the brittleness of pure ceramics. Therefore, the membrane perfectly adapts to mechanical stress, ensuring excellent flexibility for practical cell assembly.

NASICON-type LATP powder possesses a particle size of approximately 1 μm and exhibits a trigonal crystal structure (Fig. S1b and 1c). Upon heating, the epoxy groups in PEGDE undergo a curing reaction with the N–H bonds in DETA to generate a stable three-dimensional (3D) polymer network (Fig. S2b) [23]. Additionally, the Fourier transform infrared (FTIR) spectra after thermal curing reveal the disappearance of the characteristic epoxy peak in PEGDE (912 cm^{-1}) and the N–H vibration peaks in DETA (3270-3360 cm^{-1}), further confirming the reaction between the epoxy groups and N–H bonds (Fig. S3).

As depicted in Figs. 1c and 1d, owing to the wettability of the liquid polymer monomers and the substantial pressure exerted during isostatic pressing, the dense packing of LATP particles and the 3D cross-linked polymer network with exceptional mechanical properties synergistically facilitate the formation of the LATP-based film. Moreover, energy-dispersive X-ray spectroscopy (EDS) mapping results demonstrate that the LATP particles are uniformly dispersed throughout the polymer matrix (Figs.

1e and 1f). Furthermore, the incorporation of TEP not only serves as a plasticizer to enhance the ionic conductivity of the polymer segment but also improves the interfacial compatibility between LATP and PEGDE, bridging the ion-conducting channels between the polymer and LATP [24]. Finally, the NASICON structure of LATP within the film remains highly stable following the curing process of PEGDE and DETA (Fig. S4).

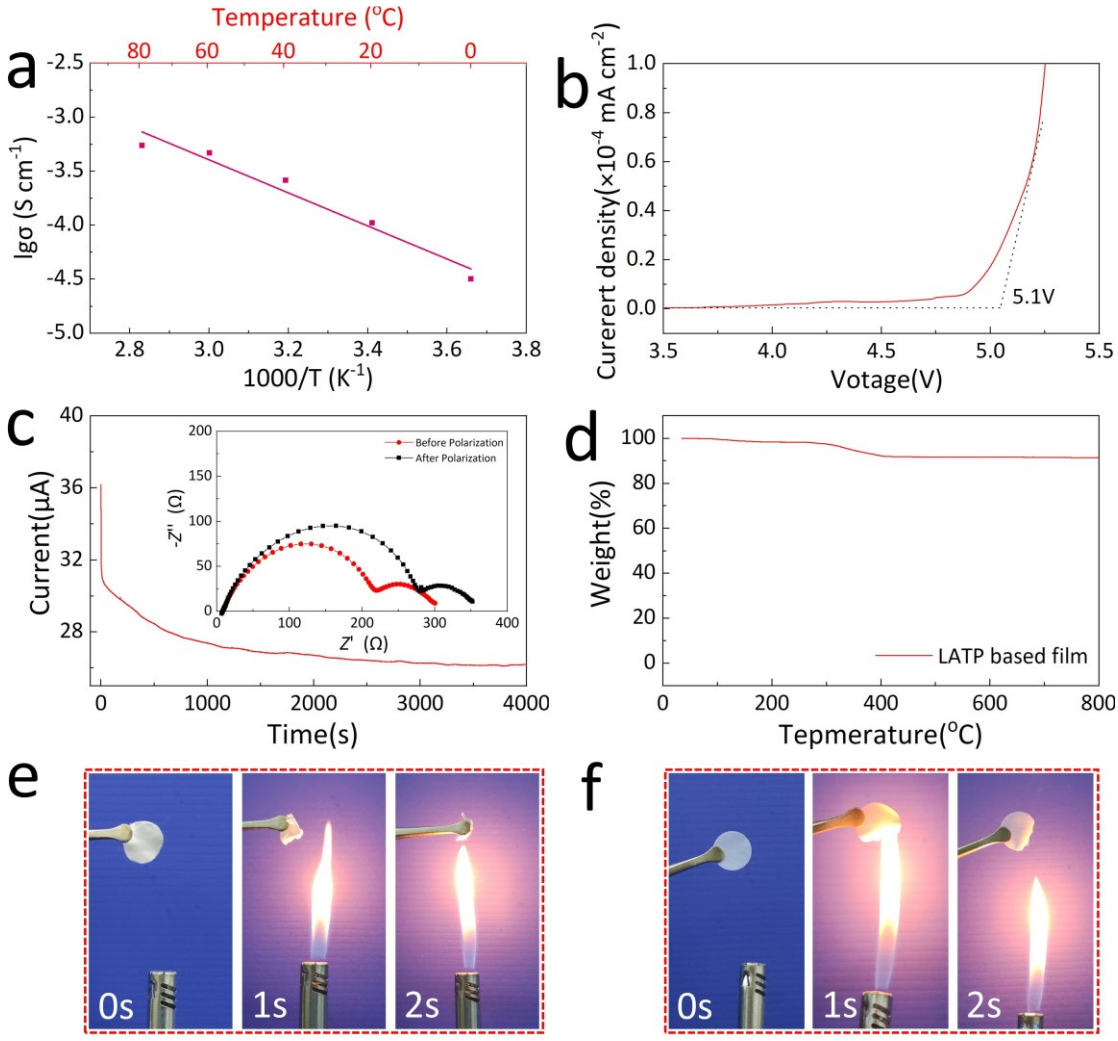


Fig. 2 (a) Arrhenius plot of the LATP-based film; (b) Linear sweep voltammetry (LSV) curve of the LATP-based film at 25 °C; (c) Polarization curve and the initial and steady-state impedance spectra (inset) of the Li| LATP-based film |Li symmetric cell; (d) Thermogravimetric analysis (TGA) curve of the LATP-based film; and flammability comparison between (e) the commercial PE separator and (f) the LATP-based film.

Owing to its ultra-thin thickness and exceptionally high ceramic content, the LATP-based film exhibits an ionic conductivity of 1.5×10^{-4} S cm^{-1} at 25 °C (Fig. S5a). The impedances of the electrolyte at various temperatures were measured (Figs. 2a and S5b). Based on the linear fitting of the data using the Arrhenius equation, the

activation energy for ion migration of the electrolyte is calculated to be merely 0.3 eV. In addition, a pure polymer electrolyte was tested as a control, which exhibited an activation energy of 0.41 eV (Figs. S5c and S5d). This result further demonstrates the significant contribution of the 90 wt% LATP ceramic phases to Li^+ transport in the composite electrolyte. As shown in Fig. S6, Li^+ transport within the LATP-based film proceeds through three synergistically coupled pathways rather than a single dominant route. At a high LATP loading of 90 wt%, the densely packed ceramic particles form an interconnected percolation network, enabling rapid Li^+ migration through the LATP bulk and across grain boundaries. Meanwhile, the conformal LATP/polymer interfaces generated by in situ curing provide additional low-resistance transport pathways, where interfacial structural and electrostatic effects may facilitate Li^+ hopping. In addition, the flexible polymer/TEP matrix infiltrates the interparticle voids, eliminates poorly contacted regions, and bridges adjacent LATP domains, thereby maintaining continuous ionic conduction throughout the film [18]. Compared with ionic conductivity, ionic conductance more accurately reflects the influence of electrolyte thickness on ion transport capability. A high ionic conductivity implies that a greater amount of Li^+ can be transported per unit time, leading to reduced ion concentration polarization during the charge/discharge process, which consequently minimizes the Ohmic impedance [24]. According to Equation S3, the ionic conductance of the 20 μm LATP-based film reaches a remarkable 14.5 mS at room temperature.

Furthermore, a wide electrochemical stability window indicates that the electrolyte is highly resistant to oxidation or reduction at elevated potentials. This enables its compatibility with high-voltage cathodes (e.g., $LiNi_{0.8}Co_{0.1}Mn_{0.1}O_2$, $LiCoO_2$, and $LiNi_{0.5}Mn_{1.5}O_4$ materials operating at > 4.3 V), thereby enhancing the energy density of the full cells. As depicted in Fig. 2b, linear sweep voltammetry (LSV) testing was conducted in a Li| LATP-based film |stainless steel half-cell. The results reveal no significant anodic current until approximately 5.1 V (vs. Li/Li^+), demonstrating that this electrolyte fulfills the requirements for coupling with high-voltage cathode materials.

The lithium-ion transference number is another crucial electrochemical parameter for the electrolyte (Fig. 2c and Table S1). Calculated using Equation S4, the transference number of the electrolyte reaches an impressive value of 0.58. A high lithium-ion transference number signifies that the majority of the current is

contributed by the migration of lithium ions, with minimal conduction from electrons or other ions (such as anions). This characteristic can significantly mitigate the risk of side reactions and alleviate concentration polarization [25].

The thermal stability of the LATP-based film was evaluated via thermogravimetric analysis (TGA) (Figs. 2d and S7). As the temperature increased from room temperature to 800 °C, the membrane exhibited a mere mass loss of approximately 10% (corresponding to the decomposition of the polymer component), indicating its robust stability at elevated temperatures. Furthermore, flammability tests (Figs. 2e and 2f) confirmed the excellent flame retardancy of the LATP-based film. Upon exposure to an open flame, the commercial PE separator was instantaneously ignited and burned vigorously. In contrast, the LATP-based film merely deformed without exhibiting any sustained combustion. The result demonstrates the intrinsic flame-retardant characteristics of the LATP-based film, holding great promise for enhancing the safety of battery systems. Collectively, these findings verify that the LATP-based film can endure high-temperature environments potentially encountered during battery operation without undergoing decomposition.

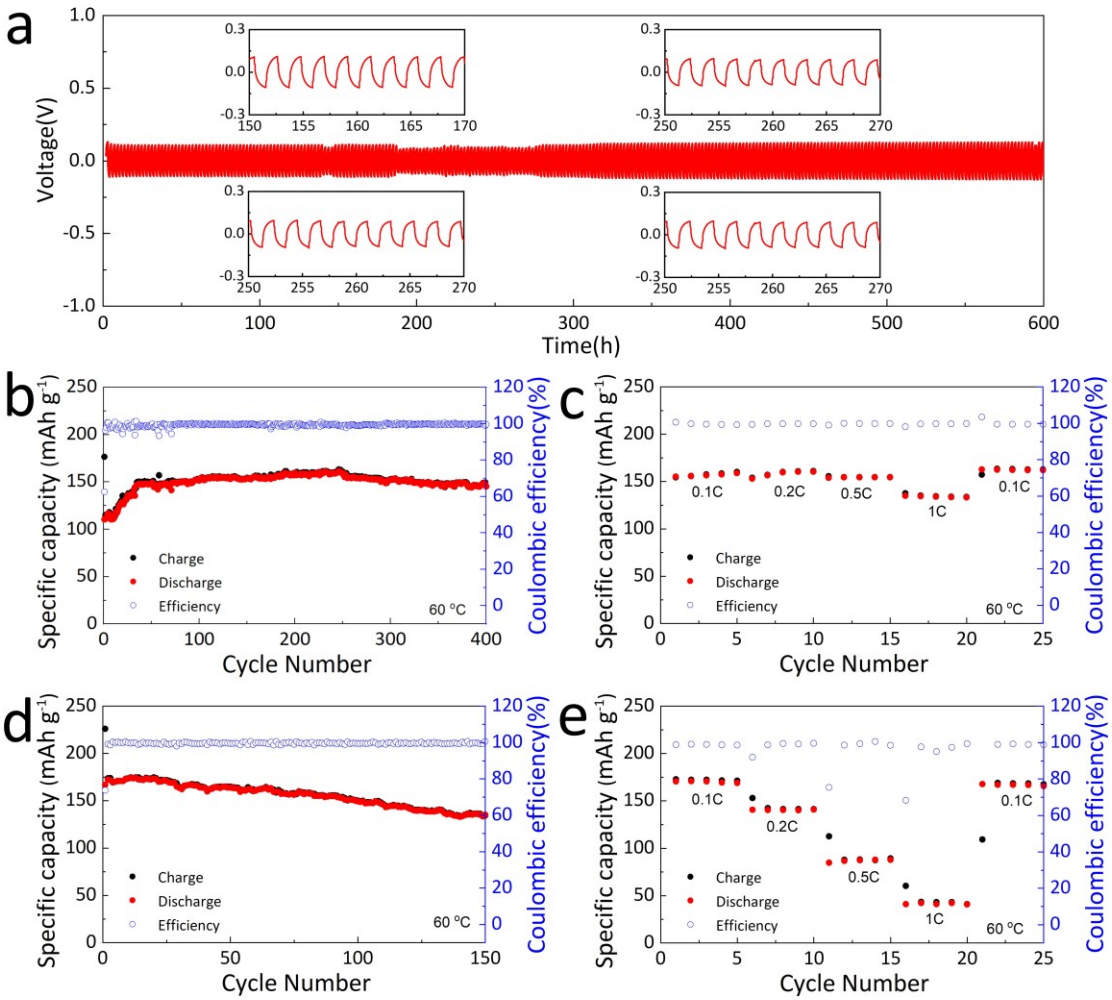


Fig. 3 (a) Galvanostatic cycling curve of the Li| LATP-based film |Li cell at 60 °C and a current density of 0.1 mA cm^{-2}; (b) Long-term cycling performance and (c) rate performance of the Li| LATP-based film |LFP cell at 60 °C and 0.1 C; (d) Cycling performance and (e) rate performance of the Li| LATP-based film |NCM811 cell at 60 °C and 0.1 C.

The cycling performance of the Li| LATP-based film |Li symmetric cell at 60 °C and 0.1 mA cm^{-2} was evaluated, as shown in Fig. 3a. The results demonstrate that during the 600 h long-term cycling, the cell exhibited a low overpotential of only 120 mV, which remained stable across all cycles (the slight overpotential fluctuations originated from testing temperature variations caused by external factors). This indicates excellent interfacial compatibility between the Li metal and the LATP-based film. By comparing the SEM images of the Li metal surface before and after cycling (Fig. S8), it can be observed that no obvious defects or dendrites appeared on the cycled Li surface, further proving the uniform deposition of Li during the cycling process. Furthermore, due to the presence of $LiNO_3$ [27], X-ray photoelectron spectroscopy (XPS) analysis of the cycled Li anode (Figs. S9a and S9b) reveals the

generation of abundant Li_3N at the LATP-based film | Li interface. Li_3N, as a critical SEI component, plays a beneficial role in improving the interfacial stability between the LATP-based film and Li metal. Notably, Ti^{4+} species in LATP are generally susceptible to reduction by metallic Li, which may produce an electronically conductive Ti^{3+}-containing interphase and thereby increase the interfacial resistance. However, as shown in Fig. S9c, only characteristic Ti^{4+} peaks are detected after cycling, with no discernible Ti^{3+} signal. These findings provide direct evidence that the reduction of Ti^{4+} is effectively inhibited.

To verify the feasibility of the LATP-based film in solid-state lithium metal batteries, LFP and NCM811 were selected as cathode materials to assemble Li| LATP-based film |LFP and Li| LATP-based film |NCM811 full cells, respectively. Fig. 3b illustrates the cycling performance of the Li| LATP-based film |LFP cell at 60 °C and 0.1 C, delivering an initial discharge specific capacity of 153.3 mAh g^{-1}. The gradual increase in capacity during the initial 50 cycles is attributed to a slow activation process [26]. After 400 cycles, the discharge specific capacity remained at 143.2 mAh g^{-1}, corresponding to a capacity retention of 93.4%. Meanwhile, the Coulombic efficiency was consistently maintained above 99% throughout the entire cycling process, indicating the outstanding cycling stability and high reversibility of the cell. To evaluate the interfacial stability between the composite electrolyte and the lithium metal anode, EIS measurements were performed on the Li symmetric cell. As shown in Fig. S10a, the initial interfacial resistance is approximately 119.5 Ω. After 200 and 400 cycles, the resistance shows only a slight increase. It stabilizes at around 169.2 Ω and 214.3 Ω, respectively. The absence of continuous impedance growth confirms that a robust protective interphase is successfully formed. This layer effectively prevents the severe reduction of LATP by Li metal, ensuring excellent long-term interfacial compatibility. Simultaneously, Fig. 3c and S10b displays the favorable rate performance of this cell. At 0.1 C, the cell can output a specific capacity of 151 mAh g^{-1}. As the C-rate increased to 1 C, the discharge specific capacity remained almost constant, with only an approximate 9% decrease at 1 C. When the C-rate returned to 0.1 C, its specific capacity recovered to the initial value.

Furthermore, the cycling performance under high-voltage conditions was evaluated using NCM811 as the cathode. As shown in Fig. 3d, at 60 °C and 0.1 C, the Li| LATP-based film |NCM811 cell delivered an initial specific capacity of 172.7 mAh g^{-1}, and a specific capacity of 133.2 mAh g^{-1} was retained after 150 cycles,

yielding a capacity retention of 77.1%. Additionally, its rate performance also demonstrated excellent results (Fig. 3e). This can be ascribed to the superior interfacial compatibility between the Li anode and the LATP-based film, as well as the robust lithium-ion migration capability facilitated by the ultra-thin electrolyte. Beyond interfacial kinetics, the ultrathin architecture of the solid electrolyte plays a decisive role in dictating the overall battery-level energy density. Because ceramic solid electrolytes inherently possess high skeletal densities (e.g., ~2.94 g cm^{-3} for LATP), a thick electrolyte layer severely burdens the passive mass and volume of the cell. To quantitatively verify the performance benefits delivered by this 20 μm membrane, a stack-level energy density model was established (details in Note S1 and Table S2). Compared to conventional composite solid electrolytes with typical thicknesses of 50–100 μm, reducing the membrane thickness to 20 μm decreases the electrolyte areal mass by up to 80% (from ~29.4 to ~5.88 mg cm^{-2}). In a practical cell configuration paired with a high-loading NCM811 cathode (3.0 mAh cm^{-2}), this thickness reduction projects an enhancement in cell-level gravimetric energy density from ~245 Wh kg^{-1} (at 100 μm) to ~351 Wh kg^{-1} (at 20 μm), accompanied by a 42% increase in volumetric energy density (from ~528 to ~752 Wh L^{-1}). While realizing these projected metrics in large-format pouch cells still calls for ongoing engineering efforts—such as optimizing roll-to-roll mechanical uniformity and addressing localized stress concentrations across larger active areas—these quantitative assessments firmly demonstrate the vital role of the 20 μm design for high-energy-density solid-state batteries.

To further evaluate the room-temperature electrochemical feasibility of the LATP-based film electrolyte, Li| LATP-based film |LFP full cells were assembled and tested at 25 °C. As shown in Fig. S11a, the cell delivered an initial discharge specific capacity of approximately 130 mAh g^{-1} at 0.1 C. During the subsequent cycling process, the discharge capacity remained relatively stable, maintaining around 125 mAh g^{-1} after 100 cycles, corresponding to a capacity retention of approximately 96%. Meanwhile, the Coulombic efficiency was maintained close to 100% throughout the cycling process, demonstrating the good reversibility and interfacial stability of the LATP-based electrolyte even under room-temperature conditions.

The rate capability of the Li| LATP-based film |LFP cell at 25 °C is presented in Fig. S11b. The cell delivered discharge capacities of approximately 135, 125, 110, and 95 mAh g^{-1} at 0.1, 0.2, 0.5, and 1 C, respectively. When the current density was

restored to 0.1 C, the capacity recovered to approximately 120 mAh g^{-1}, indicating the structural stability of the composite electrolyte during repeated charge/discharge processes. Compared with the cycling performance obtained at 60 °C, the room-temperature capacity and rate capability are relatively reduced, which can be attributed to the sluggish Li^+ transport kinetics under ambient conditions. Specifically, the ceramic-rich LATP framework provides excellent mechanical stability and electrochemical compatibility; however, the limited contribution of the polymer phase to ionic conduction and the increased interfacial resistance between ceramic particles/electrolyte and electrolyte/electrode interfaces become more pronounced at room temperature. Elevating the temperature can effectively accelerate interfacial Li^+ migration and reduce polarization, thereby enabling improved electrochemical performance at 60 °C.

3. Conclusion

In summary, a flexible LATP-based film with a thickness of 20 μm and a high ceramic content of 90 wt% was successfully fabricated via a solvent-free process. This electrolyte membrane delivers an ionic conductivity of 1.5×10^{-4} S cm^{-1} and a high ionic conductance of 14.5 mS at 25 °C. Additionally, it possesses excellent thermal stability, a wide electrochemical stability window, and a high lithium-ion transference number of 0.58. Consequently, the Li| LATP-based film |Li symmetric cell achieves stable cycling for over 600 hours at 60 °C and 0.1 mA cm^{-2}. The assembled Li| LATP-based film |LFP cell demonstrates stable cycling performance, retaining 93.4% of its capacity after 400 cycles at 0.1 C. Similarly, the Li| LATP-based film |NCM811 cell also exhibits stable cycling, yielding a capacity retention of 77.1% after 150 cycles at 0.1 C. These results demonstrate the feasibility of the LATP-based thin film electrolyte for solid-state lithium metal batteries. Furthermore, quantitative cell-level projections reveal that thinning the ceramic-rich electrolyte to 20 μm yields over a 40% enhancement in gravimetric energy density compared with conventional ~100 μm thick counterparts, highlighting its substantial promise for breaking the energy-density bottleneck of solid-state systems. Although scaling this ultrathin film from coin cells into large-format pouch cells presents practical engineering challenges in terms of large-area defect tolerance and interface stress dissipation, this work offers crucial fundamental insights into the fabrication and interfacial engineering of ultrathin, flexible composite electrolytes for next-generation solid-state lithium metal batteries. Although the LATP-based film exhibits

competitive room-temperature ionic conductivity, further enhancement of room-temperature electrochemical performance remains desirable for practical applications. This improvement can be achieved by mitigating interfacial polarization and accelerating Li-ion transport kinetics within the ceramic-rich composite framework. Future efforts will focus on optimizing polymer phase chemistry, engineering LATP/polymer interfaces, and constructing continuous low-resistance ceramic ion-conduction pathways, while preserving the intrinsic advantages of oxide-based electrolytes.

4. References

[1] Kou W, Zhang Y, Wu W, Guo Z, Hua Q, and Wang J 2024 Green Energy Environ. **9** 71-80.

[2] Pan H, Wang L, Shi Y, Sheng C, Yang S, He P, and Zhou H 2024 Nat. Commun. **15** 2263.

[3] Hu X, Zhang Z, Zhang X, Wang Y, Yang X, Wang X, Fayena-Greenstein M, Yehezkel H A, Langford S, Zhou D, Li B, Wang G, and Aurbach D 2024 Nat. Rev. Mater. **9** 305-320.

[4] Duan S, Qian L T, Zheng Y, Zhu Y F, Liu X, Dong L, Yan W, and Zhang J J 2024 Adv. Mater. **36** 2314120.

[5] Cui L, Zhang S, Ju J, Liu T, Zheng Y, Xu J, Wang Y, Li J, Zhao J, Ma J, Wang J, Xu G, Chan T-S, Huang Y-C, Haw S-C, Chen J-M, Hu Z, and Cui G 2024 Nat. Energy **9** 1084-1094.

[6] Counihan M J, Chavan K S, Barai P, Powers D J, Zhang Y, Srinivasan V, and Tepavcevic S 2024 Joule **8** 64-90.

[7] Li J, Hu Z, Zhang S, Zhang H, Guo S, Zhong G, Qiao Y, Peng Z, Li Y, Chen S, Chen G, and Cao A-M 2024 Nat. Sustain. **7** 1481-1491.

[8] Ahuis M, Doose S, Vogt D, Michalowski P, Zellmer S, and Kwade A 2024 Nat. Energy **9** 373-385.

[9] Liu M, Song A, Zhang X, Wang J, Fan Y, Wang G, Tian H, Ma Z, and Shao G 2025 Nano Energy **136** 110749.

[10] Wang D, Gwalani B, Wierzbicki D, Singh V, Jhang L-J, Rojas T, Kou R, Liao M, Ye L, Jiang H, Shan S, Silver A, Ngo A T, Du Y, Li X, and Wang D 2025 Nat. Mater. **24** 243-251.

[11] Guo S, Tan S, Ma J, Chen L, Yang K, Zhu Q, Ma Y, Shi P, Wei Y, An X, Ren Q, Huang Y, Zhu Y, Cheng Y, Lv W, Hou T, Liu M, He Y-B, Yang Q-H, and Kang F 2024 Energy Environ. Sci. **17** 3797-3806.

[12] Zhang S, Li Y, Bannenberg L J, Liu M, Ganapathy S, and Wagemaker M 2024 Sci. Adv. **10** eadj8889.

[13] Wang Z, Xia J, Ji X, Liu Y, Zhang J, He X, Zhang W, Wan H, and Wang C 2024

Nat. Energy **9** 251-262.
[14] Zhang Z, and Han W-Q 2023 Nano-Micro Lett. **16** 24.
[15] Li B, Wang C, Yu R, Han J, Jiang S, Zhang C, and He S 2024 Energy Environ. Sci. **17** 1854-1884.
[16] Da X Y, Chen J, Qin Y Y, Zhao J Y, Jia X, Zhao Y J, Deng X T, Li Y N, Gao N, Su Y Q, Rong Q, Kong X P, Xiong J Q, Hu X F, Ding S J, and Gao G X 2024 Adv. Energy Mater. **14**.
[17] Zou S, Yang Y, Wang J, Zhou X, Wan X, Zhu M, and Liu J 2024 Energy Environ. Sci. **17** 4426-4460.
[18] Chen L, Li Y, Li S-P, Fan L-Z, Nan C-W, and Goodenough J B 2018 Nano Energy **46** 176-184.
[19] Huo H Y, Chen Y, Luo J, Yang X F, Guo X X, and Sun X L 2019 Adv. Energy Mater. **9** 1804004.
[20] Yang H, Jing M, Wang L, Xu H, Yan X, and He X 2024 Nano-Micro Lett. **16** 127.
[21] Peng H, Long T R, Peng J, Chen H, Ji L F, Sun H, Huang L, and Sun S G 2024 Adv. Energy Mater. **14** 2400428.
[22] Su X, Xu X-P, Ji Z-Q, Wu J, Ma F, and Fan L-Z 2024 Electrochem. Energy Rev. **7** 2.
[23] Guo Q, Xu F, Shen L, Deng S, Wang Z, Li M, and Yao X 2022 Energy Mater. Adv. **2022** 9753506.
[24] Jiang S P 2022 Electrochem. Energy Rev. **5** 21.
[25] Zhu Q, Ma J, Li S, and Mao D 2023 Polymers (Basel) **15** 2469.
[26] Wang J, Yang J, Shen L, Guo Q, He H, and Yao X 2021 ACS Appl. Energy Mater. **4** 4129-4137.